ADVANCED MATERIALS INTERFACES
www.advmatinterfaces.de

A Nanocellulose-Paper-Based SERS Multiwell Plate with High Sensitivity and High Signal Homogeneity

*Longyan Chen, Binbin Ying, Pengfei Song, and Xinyu Liu**

Paper-based surface-enhanced Raman scattering (SERS) substrates have gained growing interest as an eco-friendly and low-cost tool for chemical and biosensing. However, paper-based SERS substrates often suffer relatively low signal spatial homogeneity because of their nonuniform hot-spot distribution. In this paper, a nanofibrillated cellulose paper (nanopaper) based SERS multiwell plate is developed for trace chemical detection with high sensitivity and high signal homogeneity. The SERS plate is fabricated from ultrasmooth (2,2,6,6-tetramethylpiperidin-1-yl)oxyl-oxidized NFC paper (TO-nanopaper) through wax-printing-based multiwell patterning followed by silver nanoparticle (AgNP) growth based on a successive ionic layer adsorption and reaction (SILAR) process. Taking advantage of the abundance of carboxyl groups on the TO-nanopaper, uniformly distributed and densely arranged AgNPs are successfully synthesized through the SILAR process on the NFC multiwell surface under ambient conditions. The SERS performance of the device is evaluated for testing two Raman marker chemicals, rhodamine B and 2-naphthalenethiol, and picomolar detection limit and high Raman enhancement factor (up to 1.46×10^9) are achieved. The Raman signal mapping results show superior signal spatial homogeneity of the device with low variations (≤11%). The nanopaper-based SERS device represents a promising SERS platform for chemical and biomolecule detections with high sensitivity and high repeatability.

1. Introduction

Surface-enhanced Raman scattering (SERS) is one of the most attractive analytical methods for label-free, high-sensitivity detection of biological and chemical analytes.[1–4] In SERS, the Raman signal intensity can be enhanced by several orders of magnitude through local amplification of the electromagnetic field in the close proximity of a SERS substrate,[5] which is typically a nanostructured metal surface. Various SERS substrates have been constructed from nanostructured metal materials on a rigid support such as glass,[6,7] silicon wafer,[8,9] and aluminum films,[10,11] through fabrication techniques such as lithography[12,13] and chemical synthesis.[14–16] These micro and nanofabricated substrates are usually of high sensitivity and signal spatial homogeneity due to the uniform distribution of hot spots on their surfaces. However, the fabrication of these SERS substrates typically involves sophisticated facilities and requires a long preparation time. There remains a strong need to develop low-cost SERS substrates and devices, with high sensitivity and signal spatial homogeneity, through simple and efficient fabrication techniques.

In the past decade, cellulose paper has been demonstrated as a low-cost, disposable, and biodegradable substrate material for chemical and biochemical analysis in the format of microfluidic paper-based analytical device (μPAD).[17–20] There is a particular interest in incorporating nanomaterials on paper-based devices for SERS-based chemical and biosensing.[21–27] In most cases, paper-based SERS substrates were fabricated by depositing presynthesized noble metal nanoparticles (NPs) on commercial filter paper or chromatography paper via directly loading,[22,24,25] inkjet printing,[26] or screen printing.[27] The porous and 3D structure of cellulose paper has been utilized for capillarity-driven separation and preconcentration of analytes and thus enhancement of the SERS sensitivity.[21,22,25–27] However, the 3D porous surface topologies, which are typically distributed randomly during cellulose paper manufacturing, also caused nonuniform distribution of the deposition/formation of nanoplasmonic structures (SERS hot spots) on the paper surface and thus relatively low spatial homogeneity of the SERS intensities across the substrate.[25] A larger laser spot was usually applied to the cellulose paper substrate for SERS signal measurement

Dr. L. Chen, B. Ying, Dr. P. Song, Prof. X. Liu
Department of Mechanical Engineering
McGill University
817 Sherbrooke Street West, Montreal, QC H3A 0C3, Canada
E-mail: xyliu@mie.utoronto.ca
Dr. L. Chen
Alentic Microscience Inc.
1344 Summer Street, Halifax, NS B3H 0A8, Canada
B. Ying, Dr. P. Song, Prof. X. Liu
Department of Mechanical and Industrial Engineering
University of Toronto
5 King's College Road, Toronto, Ontario M5S 3G8, Canada
Dr. P. Song
Department of Electrical and Electronic Engineering
Xi'an Jiaotong-Liverpool University
111 Ren'ai Road, Suzhou 215123, P. R. China
Prof. X. Liu
Institute of Biomaterials and Biomedical Engineering
University of Toronto
164 College Street, Toronto, Ontario M5S 3G9, Canada

The ORCID identification number(s) for the author(s) of this article can be found under https://doi.org/10.1002/admi.201901346.

DOI: 10.1002/admi.201901346

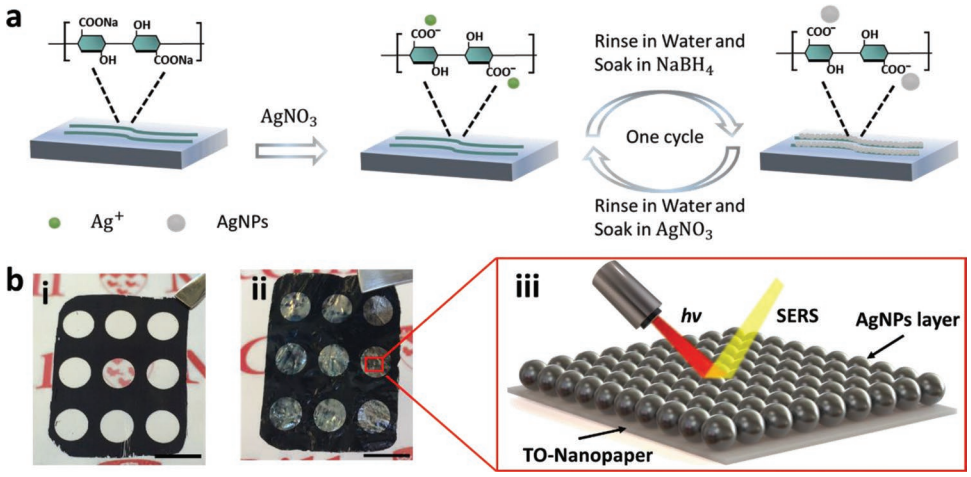

Figure 1. AgNP synthesis on TEMPO-oxidized nanopaper (TO-nanopaper) based multiwell plate. a) Schematic illustration of AgNP growth on TO-nanopaper through the SILAR process. b) Photographs of TO-nanopaper-based multiwell plate (i) before and (ii) after one cycle of AgNPs growth (scale bar: 1 cm). b-iii) Schematic illustration of the SERS-based molecule detection on the TO-nanopaper-based SERS substrate.

to achieve better signal homogeneity through spatial averaging of the intensity variations, which however led to reduced sensitivity.

Recently, nanofibrillated cellulose (NFC) paper has emerged as a promising substrate material for fabricating analytical and electronic devices.[28–30] Compared to cellulose paper, NFC paper (simply called "nanopaper" in this work) possesses densely packed cellulose nanofibers and nanometer-sized pores, resulting in its excellent mechanical properties, high optical transparency, ultrasmooth surface, and homogeneous distribution of surface chemical groups.[30] Several studies have explored the incorporation of metal NPs into the nanopaper as SERS substrates via thermal synthesis,[31,32] UV irradiation,[33] and filtration.[34,35] Without analyte preconcentration, however, these nanopaper-based SERS substrates typically provide medium-level sensitivity (e.g., at the nanomolar level), which is partially due to the relatively low NP density on the nanopaper produced by the employed fabrication techniques.

In this study, a novel SERS multiwell plate was fabricated from ultrasmooth nanopaper through multiwell patterning by wax printing and silver NP (AgNP) synthesis by a facile successive ionic layer absorption and reaction (SILAR) process. The nanopaper-based SERS multiwell plate enables trace chemical detection with high sensitivity and high signal spatial homogeneity (signal uniformity across different locations of the SERS plate). Different from previous reports,[28,31,34,35] AgNPs were synthesized, for the first time, directly on (2,2,6,6-tetramethylpiperidin-1-yl)oxyl (TEMPO)-oxidized NFC paper (TO-nanopaper) under ambient conditions. A continuous layer of uniformly distributed and densely arranged AgNPs was formed on the TO-nanopaper through the SILAR process, thanks to the ultrasmooth surface and abundant carboxyl groups on the TO-nanopaper. The entire fabrication process of our nanopaper-based SERS multiwell plate is rapid, low-cost, and highly efficient, providing a new solution for high-performance SERS-based chemical analysis and biosensing. The SERS plate was demonstrated for the detection of two chemical Raman reporters—Rhodamine B (RhB) and 2-naphthalenethiol (2-NT), and the plate's analytical performance was evaluated. The results show limits of detection (LODs) of 1×10^{-12} M for RhB and 172×10^{-12} M for 2-NT, which are lower than those of existing nanopaper-based SERS substrates. We also demonstrated that our nanopaper-based SERS plate provided enhanced signal homogeneity over that of regular cellulose paper-based SERS substrate.

2. Results and Discussions

2.1. AgNP Growth Efficiency on Different Paper Substrates

We prepared two types of nanopaper substrate from commercially available NFC nanofibers (i.e., regular NFC nanofiber and TEMPO-NFC nanofibers with mean diameters of ≈50 and ≈10 nm, respectively, as instructed in manufacturer production information, as well shown in Figure S1, Supporting Information) through a vacuum filtration process. We first investigated the efficiency of AgNP growth on the three types of paper substrate (cellulose filter paper, regular nanopaper, and TO-nanopaper) through the SILAR process. Each cycle of the SILAR process (**Figure 1**a) involved successive immersions of the paper substrate in the precursor silver nitrate ($AgNO_3$) solution, deionized (DI) water, the reductant sodium borohydride ($NaBH_4$) solution, and DI water again. Ag seeds were first formed by reducing Ag^+ absorption on the paper surface with BH_4-. Over the successive cycles, AgNPs were grown from the seeds to a densely packed layer on the paper surface. Figure 1b shows a TO-nanopaper-based 3 × 3 well plate before and after one SILAR cycle. The SERS analysis was conducted on each paper well, as schematically shown in Figure 1b-iii. The morphology and distribution of the AgNPs on the three types of paper substrate after five SILAR cycles were characterized by scanning electron microscope (SEM). **Figure 2**a shows that the cellulose filter paper was well covered with AgNPs. The growth efficiency of AgNPs on the regular nanopaper was significantly lower than that on the cellulose filter paper, and

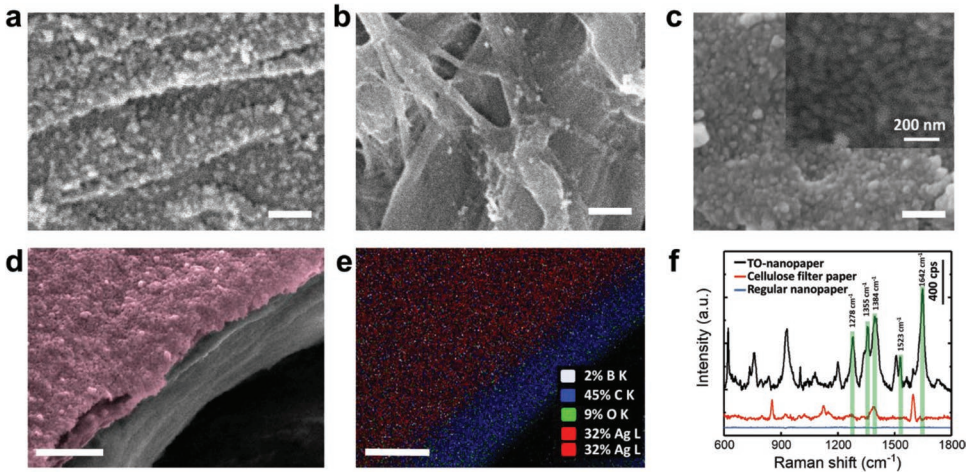

Figure 2. Characterization of AgNPs grown on different types of paper. SEM photographs of AgNPs on a) commercial cellulose filter paper, b) regular nanopaper (without TEMPO oxidization), and c,d) TO-nanopaper. The AgNP layer in (d) was pseudo-colored in pink. e) Energy-dispersive X-ray spectrometry (EDS) mapping result of the substrate shown in (d). f) Raman spectra of 1×10^{-6} M RhB solution on the three types of SERS substrate. The number of SILAR cycles was five for all three types of paper substrate. Scale bar in (a–c): 500 nm. Scale bar in (d, e): 2 µm.

only a sparse distribution of the AgNPs was observed on the regular nanopaper after five SILAR cycles (Figure 2b). Different from the cellulose filter paper and the regular nanopaper, the TO-nanopaper gained an evenly distributed, densely arranged layer of AgNPs (Figure 2c,d). It should be noted that Figure 2c,d show the AgNPs distribution profile after five SILAR cycles, of which Raman signal was found most significantly enhanced (as discussed in Section 2.2). After just one SILAR cycle, we still observed a densely arranged AgNP layer formed on the TO-nanopaper (Figure S5a, Supporting Information), which confirms the high efficiency of AgNP growth on the TO-nanopaper.

Previous reports have demonstrated that the SLIAR-based AgNP growth was significantly affected by the Ag^+ adsorption capacity of the substrate,[23,36] which highly depends on the substrate surface morphology and chemistry. The cellulose filter paper comprises cellulose microfibers (diameter ≈ 20 µm) and exhibits a 3D porous structure (Figure S2a, Supporting Information). Therefore, the cellulose filter paper was able to keep the $AgNO_3$ solution inside its 3D porous structure and thus hold the reduced Ag seeds after its immersion into the $NaBH_4$ solution, eventually resulting in the coating of AgNPs on its cellulose microfibers after successive SILAR cycles (Figure 2a). In contrast, both regular nanopaper and TO-nanopaper possess densely packed cellulose nanofibers with nanometer-sized pores (Figure S2b–d, Supporting Information), which limits the absorption of Ag^+ on their surfaces through their porous structures. However, the TO-nanopaper made from TEMPO-treated NFC contains a large number of negatively charged carboxyl groups (carboxylate concentration of 1.4 mmol g^{-1} solid, according to the manufacturer's datasheet), which do not exist on the regular nanopaper.[37] As a result, the TO-nanopaper can efficiently absorb Ag^+ on its surface through electrostatic interaction of the Ag^+ and carboxyl groups,[38] leading to a high growth rate between AgNPs. For the regular nanopaper, the hydroxyl groups in the D-glucose unit of the non-TEMPO-oxidized NFC surface have relatively lower affinity to Ag^+,[38] which accounts for the low AgNP growth efficiency on the regular nanopaper. Another possible reason for the high AgNP growth efficiency of the TO-nanopaper is that the carboxylate groups on the TO-nanopaper surface could serve as docking sites to stabilize the AgNPs on its surface.[39]

The AgNPs were grown on the TO-nanopaper after five SILAR cycles have a diameter of 67 ± 18 nm, as shown in the histogram inset of Figure S5c (Supporting Information). The UV–vis absorption spectrum shows two surface plasmon absorption peaks at 422 and 524 nm (Figure S3a, Supporting Information) on the AgNPs-coated TO-nanopaper (after background-subtracted from bare TO-nanopaper). The first peak is the absorption of AgNPs with diameter around 50 to 60 nm, which account for the major contribution to SERS enhancement.[40] The second broad absorption peak at a longer wavelength (524 nm) could be due to the formation of AgNPs with sizes larger than 80 nm as SILAR cycles increasing.[41] The AgNP layer grown on the TO-nanopaper was further confirmed by energy-dispersive X-ray spectrometer (EDS) mapping of the cross section of the AgNP-coated TO-nanopaper (Figure 2d,e) and by X-ray photoelectron spectroscopy (XPS) analysis of the AgNP layer (Figure S3b, Supporting Information). The EDS mapping result reveals a distinctive Ag layer (red dots in Figure 2e) existing on the TO-nanopaper top surface but not on its cross section. It should be noted that the elements dot-based SEM-EDS may not show individual particle for the densely packed nanoparticles, as there are also other silver particles beneath the superficial silver particles and gaps. The XPS spectrum in Figure S2b (Supporting Information) also shows strong Ag3d peaks indicating the presence of AgNPs on the TO-nanopaper surface.

We also performed SERS measurements of RhB solution (1×10^{-6} M) dropped onto the SERS paper wells made from the three types of paper substrate. Figure 2f shows the Raman spectra measured on the three different types of paper well based on same number of growth cycles (five cycles), among which the spectrum measured from the TO-nanopaper well contains strong RhB bands including C—O—C stretching (1278 cm^{-1}), C—C stretching (1355 cm^{-1}), C—N stretching

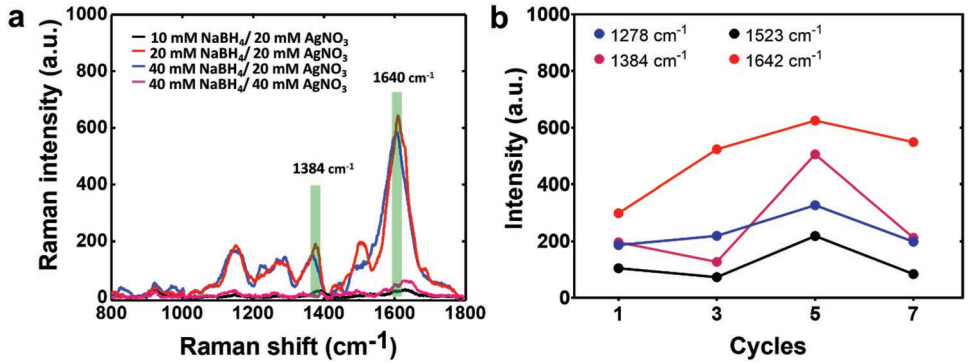

Figure 3. Optimization of the SILAR conditions for AgNP growth on TO-nanopaper. a) Raman spectra of 1×10^{-6} M RhB measured from TO-nanopaper with AgNPs grown with different concentrations of $NaBH_4$ and $AgNO_3$. b) Raman intensities of the four RhB characterization peaks measured from TO-nanopaper with AgNPs grown with different numbers of SILAR cycle (20×10^{-3} M $NaBH_4$ and 20×10^{-3} M $AgNO_3$).

(1384 cm^{-1}), C—H stretching (1523 cm^{-1}), and aromatic C—C stretching (1642 cm^{-1}).[42] The detailed tentative band assignments are listed in Table S1 (Supporting Information). As expected, the regular nanopaper well with sparse AgNP coating provides weak Raman signals (Figure 2f). Because of its higher AgNP coating density, the cellulose filter paper well has higher Raman signal intensities at the abovementioned RhB peaks than those from the regular nanopaper well. The Raman intensities measured from the TO-nanopaper well proved to be the highest, confirming that the densely arranged AgNPs provided abundant active hot spots for significant Raman enhancement.

2.2. Optimization of AgNP Growth Conditions on TO-Nanopaper

To improve the SERS sensitivity of the nanopaper-based SERS plate, we optimized the SILAR conditions including the reagent concentrations and the number of reaction cycles. Based on previously reported SLIAR protocols,[23,36] we adjusted concentrations of the $AgNO_3$ and $NaBH_4$ solutions in the range of 10×10^{-3}–40×10^{-3} M. One SILAR cycle was performed to determine the most efficient solution concentrations for AgNP growth, as one cycle could readily generate a continuous layer of densely arranged AgNPs on the TO-nanopaper with good Raman enhancement. We measured Raman spectra of 1×10^{-6} M RhB solution added to TO-nanopaper wells with AgNPs grown under different combinations of $AgNO_3$ and $NaBH_4$ concentrations (**Figure 3**a), and found that the combination of 20×10^{-3} M $NaBH_4$ and 20×10^{-3} M $AgNO_3$ produced the highest Raman intensities at distinctive bands of 1384 and 1642 cm^{-1} (blueshifted in the blue and red spectrum curves in Figure 3a). An interesting observation in our experiments is that high concentrations of both solutions (at 40×10^{-3} M) did not lead to higher Raman intensities. In SERS, the Raman enhancement depends on the metallic particle size (optimal diameter: 50–60 nm for AgNPs) and interparticle spacing (optimal distance: <10 nm).[43,44] The reduction step (in the $NaBH_4$ solution) in our SILAR process is expected to be fast due to a large amount of Ag^+ adsorbed on TO-nanopaper; during this fast reaction, a significant amount of $NaBH_4$ is required to passivate particle surface and stabilize AgNPs.[45] Figure S3a (Supporting Information) shows that large AgNPs (average diameter ≈202 nm) were formed at a low $NaBH_4$ concentration (10×10^{-3} M $NaBH_4$ and 20×10^{-3} M $AgNO_3$), which might be due to the inefficient passivation of AgNP surface by $NaBH_4$. This large AgNP size caused the low Raman intensities (Figure 3a). Thus, a relatively high $NaBH_4$ concentration is required to expedite the reaction and reduce the AgNP size. However, further increase of the $NaBH_4$ concentration did not give significant enhancement of the Raman signal intensities, which is evidenced by the similar spectrum curves with concentration combinations of 20×10^{-3} M $NaBH_4$/20×10^{-3} M $AgNO_3$ (red curve) and 40×10^{-3} M $NaBH_4$/20×10^{-3} M $AgNO_3$ (blue curve) in Figure 3a. In the meanwhile, a suitable concentration of $AgNO_3$ is also needed to avoid the reaction running either too fast (which results in fusion of the AgNPs and thus less "hot spots," as shown in Figure S4c, Supporting Information) or too slow (which results in large particle sizes, as shown in Figure S4d, Supporting Information). Therefore, the concentration combination of 20×10^{-3} M $NaBH_4$ and 20×10^{-3} M $AgNO_3$ was chosen for further experiments.

We also investigated the effect of the number of SILAR cycles on the enhancement of Raman intensities. Figure 3b shows the Raman intensities in the four characterization bands of RhB in response to the number of SILAR cycles. It was found that slightly higher Raman band intensities could be achieved on the AgNPs grown with more SILAR cycles. The five-cycle condition yielded the highest Raman signal enhancement, and further increase to seven cycles did not provide further Raman signal enhancement. This could be explained from SEM images shown in Figure S5 (Supporting Information). As mentioned before, one SILAR cycle could generate a well AgNPs layer on TO-nanopaper due to high efficiency of the reaction. Increasing growth cycles from 1 to 5 generally leads to the growth of more AgNPs with diameter around 50 to 60 nm from seeds (histograms from Figure S5a–c, Supporting Information), which could account for the higher band intensity in cycle 5. However, it is also observed that few large and nonspherical AgNPs appeared with the increase of cycle number (Figure S5c, Supporting Information). Large particles formed probably due to fusion of two or more particles during Ag growth reaction. Particularly, further increasing the cycle number to 7 leads to formation of large sub-micrometer AgNP clumps (Figure S5d,

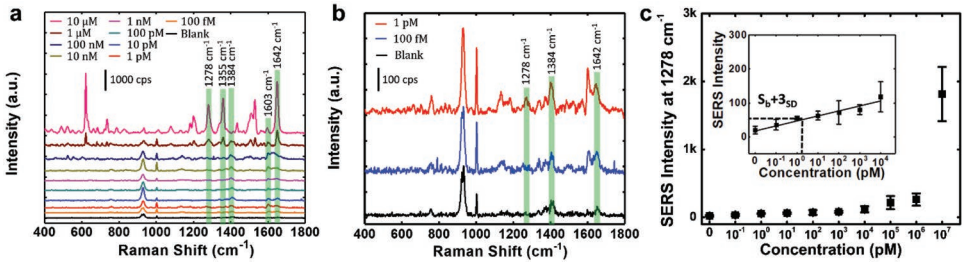

Figure 4. SERS-based detection of RhB on the TO-nanopaper-based SERS multiwell plate. a) Raman spectra measured from RhB at concentrations of 100×10^{-15} to 10×10^{-6} M. b) Detailed Raman spectra at low concentrations of RhB. c) Calibration plot of the SERS signal intensity at 1278 cm^{-1} versus the RhB concentration ($n = 3$). The fitted linear curve in the range of 0–10×10^{-9} M was $y = 6.21 \times \ln(x) + 49.19$ ($R^2 = 0.95$).

Supporting Information), which could reduce the interparticle spacing and therefore the number of "hot spots", and hence result in Raman signal drop at that point. We thus choose five cycle as the reaction condition to prepare substrates for further experiments.

Under the aforementioned optimized conditions, it is clearly that a densely packed AgNPs-based layer grown on the surface of TO-nanopaper and the uniform space between particles were visible, as shown in Figure S4b (Supporting Information) (for 20×10^{-3} M $NaBH_4$/20×10^{-3} M $AgNO_3$) and Figure S5a–c (Supporting Information) (for 1 to 5 cycles), respectively. A silvery reflectance was observed in our TO-nanopaper-AgNPs device (Figure 1b-ii). It should be noted that the densely packed AgNPs layer (or film) is different from bulk silvery Ag film, where the basic unit of the former is individual nanosized particles while the latter is based directly on atoms or molecules. The silvery reflectance indicated the reflectance of light at visible range. Yen et al.[46] predicted that the reflection peak of a single (or few) AgNP appeared near its localized surface plasmon resonance (LSPR), and showed that the LSPR spectrum was affected by the particle size and density. As the number of AgNPs increased, the reflection peak experienced a redshift with the increase of reflective power due to a coupling effect occurred between AgNPs. The reflective power further increased, and the peak moved to longer wavelengths when numerous closely packed particles formed a continuous NP film.[46] The coupling effect in densely packed NP system due to dipole–dipole interaction between neighboring nanoparticles was also described in effective medium theories by adjusting the classical Mie theory.[47,48] As a result, the reflectance in a densely packed NP system was high with a dip at the LSPR wavelength where the LSPR absorption was dominant over spectral reflection.[46,49] In the meanwhile, the LSPR absorption wavelength is proportional to particles size. With a decrease in the particle size, the LSPR effect peak moves to short wavelength, together with the prominent increase of the dip in reflection spectral and the significant decrease of reflectance power.[49,50] Large AgNPs (>50 nm) exhibit a broad LSPR spectrum with peaks at the longer wavelength regime and show higher reflectance over a broad wavelength range (across the visible range), leading to the silvery white reflectance color as reported in our study (as showed in Figure 1b-ii), as well as in other studies.[46,49,51]

It should be noted that the model and approaches mentioned before are based on a continuous AgNPs layer or a monolayer, which requires a flat surface, to support the AgNPs layer. The increase of surface roughness causes the decrease of reflectance at short wavelength due to scattering loss in the regime. In our study, the superior smooth TO-nanopaper (Figure S2c–e, Supporting Information) provides a flat surface for a continuous AgNPs film, which may thus stabilize the reflectance. The thickness of film can also affect the reflectance color. A thin film would be insufficient to reflect the light in longer wavelength regime. A thickness of AgNPs film above 450 nm provides a broad reflectance wavelength.[52] In our study, owing to the abundance of COOH group on the TO-nanopaper and a fast reaction rate, we synthesized a thick AgNPs layer (thickness of ≈600 nm at the optimized condition, Figure S3c, Supporting Information). Overall, the combination of the densely packed continuous AgNP film, the thickness and the particle size (average diameter at ≈67 nm) may cause the silvery reflectance of the AgNPs film in this study.

2.3. Evaluation of SERS Performance

We then evaluated the SERS sensing performance of our TO-nanopaper-based multiwell plate, which was prepared under the optimized SILAR conditions (20×10^{-3} M $AgNO_3$, 20×10^{-3} M $NaBH_4$, and 5 growth cycles). We analyzed two model Raman reporters, RhB and 2-NT, which are believed to interact with AgNPs through electrostatic interaction[53] and strong chemical absorption bond (semicovalent bond),[54] respectively. **Figure 4**a shows the RhB Raman spectra at various concentrations (100×10^{-15} to 10×10^{-6} M) in ethanol, and pure ethanol was used as blank control. Prominent characteristic Raman bands (1278, 1355, 1384, 1603, and 1642 cm^{-1}) of the RhB were found in RhB samples at all concentrations (Figure 4a). Figure 4b illustrates the detailed spectra at low RhB concentrations, and clear Raman intensity enhancement can be observed at the Raman bands of 1278, 1384, and 1642 cm^{-1} between the spectra of the 100×10^{-15} M sample and the blank. The 1278 cm^{-1} band was selected as the analytical marker, as this band intensity was more sensitive to RhB concentration with lower background noise (Figure 4b). Using the 1278 cm^{-1} peak intensity as the readout, we obtained the calibration curve of RhB detection (Figure 4c). The curve is monotonic to the concentration. The LOD was found to be 1.3×10^{-12} M, which was defined as the RhB concentration corresponding to the blank control intensity plus three times of the standard deviation of the Raman

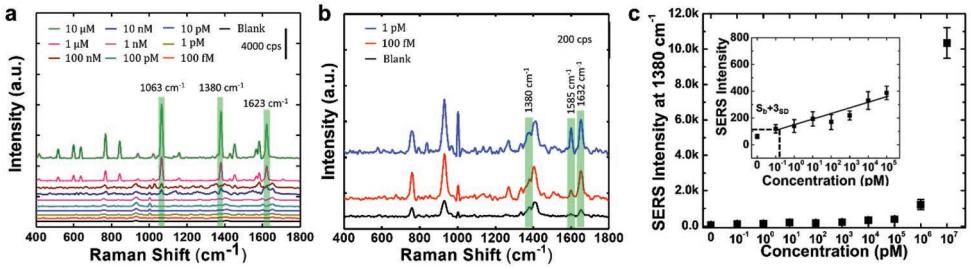

Figure 5. SERS-based detection of 2-NT on the TO-nanopaper-based SERS plate. a) Raman spectra measured from 2-NT at concentrations of 10×10^{-15} to 10×10^{-6} M. b) Detailed Raman spectra at low concentrations of 2-NT. c) Calibration plot of the SERS signal intensity at 1380 cm^{-1} versus the 2-NT concentration. The fitted linear curve in the range of 0.1×10^{-12} to 100×10^{-15} M was $y = 18.554 \times \ln(x) + 138.67$ ($R^2 = 0.92$).

intensity from the blank control. The linear range based logarithmic form of the RhB detection on our device was 0–100×10^{-9} M ($R^2 = 0.93$).

The 2-NT molecule is known for its strong affinity with noble metal surfaces.[54] **Figure 5**a,b shows the Raman spectra of 2-NT at different concentrations. The intensities of the prominent bands of 2-NT (1063, 1380, and 1623 cm^{-1}) increased with the 2-NT concentration. From Figure 5b, one can observe clear Raman enhancement at peaks of 1380, 1585, and 1623 cm^{-1} for 100×10^{-15} M 2-NT. Since the 1380 cm^{-1} peak (ring stretching) was more representative at all the concentrations and also used as a typical analytical marker in another study,[55] it was chosen for generating the calibration curve of 2-NT detection (Figure 5c). The LOD was calculated to be 172×10^{-15} M, and the linear range was 0.1×10^{-12} to 100×10^{-9} M ($R^2 = 0.92$).

It seems that the linearity in our current TO-nanopaper SERS substrate is at low concentrations and lost at high concentration (>1×10^{-6} M). It should be noted that due to the uniform surface of TO-nanopaper, the sample drop tends to distribute homogenously across the multiple well (6 mm in diameter). This may cause that at low concentration, most of the laser spot (with diameter of 25 μm) reporting few molecules adsorbed on AgNPs (estimated 80–100 molecules for a solution with concentration of 1×10^{-12} M) and even less trapped in "hot spot" which overall limit our assay detection limit, whereas at higher concentrations for the same illuminated spot, the molecules adsorbed on AgNPs and trapped in the "hot spot" increase dramatically, causing nonlinear digital. In such a case, we would wish in our future work to further improve the assay sensitivity by increasing density of molecules to be adsorbed on our devices, such as tuning device geometric size and shape, chemical modification of the naked AgNPs to enhance adsorption of molecules accordingly,[56,57] or integrating with analytes preconcentration unit by using paper (nanopaper)-based microfluidic technology.[58,59]

To evaluate the SERS activity on our TO-nanopaper-based multiwell plate, the Raman enhancement factor (EF) was calculated from the RhB detection results based on[60]

$$\mathrm{EF} = \frac{I_{\mathrm{SERS}}}{I_{\mathrm{bare}}} \times \frac{C_{\mathrm{bare}}}{C_{\mathrm{SERS}}} \quad (1)$$

where I_{SERS} and I_{bare} are the intensities of the selected scattering bands in the Raman spectra with and without SERS effect, respectively, and C_{bare} and C_{SERS} are the RhB concentrations on bare TO-nanopaper (without AgNPs) and AgNP-coated TO-nanopaper well, respectively. Based on intensities at the 1380 cm^{-1} band, $I_{\mathrm{SERS}} = 14.009$ (original intensity subtracted by that SERS substrate without RhB) for RhB of $C_{\mathrm{SERS}} = 1 \times 10^{-12}$ M on the AgNP-coated TO-nanopaper well, and $I_{\mathrm{bare}} = 9.6$ for RhB of $C_{\mathrm{SERS}} = 1 \times 10^{-3}$ M on the bare TO-nanopaper. Therefore, the EF was calculated to be 1.46×10^9, which is comparable to that of the reported paper-based SERS substrates with high sensitivities.[23] The result indicates that our TO-nanopaper SERS substrate holds significant potential for sensitive analytical assays.[60]

2.4. Homogeneity Testing of the Raman Signal

One of the main characteristics of an ideal SERS substrate is the high spatial homogeneity of the Raman signal. Although the regular cellulose paper has been demonstrated for low-cost and high-performance SERS substrates, one inherent drawback of the cellulose-paper-based SERS substrates is their signal inhomogeneity over the substrate surface because of the microscale porous structures of the cellulose paper. The porous, 3D surface morphology of the cellulose-paper-based SERS substrate could cause out-of-focus excitations by the incident laser on hot spots at different heights on the substrate surface and hence result in large spatial variations of the Raman intensity measured over the substrate.[25]

We performed confocal Raman mapping to characterize the spatial homogeneity of SERS signals from 1×10^{-6} M 2-NT on cellulose filter paper and TO-nanopaper SERS substrates (both prepared under the optimized SILAR conditions). **Figure 6**a shows the Raman intensity map of a 50×50 μm^2 area on the AgNP-coated cellulose paper at the peak of 1380 cm^{-1} (a redshift observed), in which many "islands" with high SERS signal intensities were surrounded by "blue sea" areas with very low intensities. The high-intensity "islands" could be due to the less porous junctions and knots of cellulose microfiber in the paper on which the incident laser was more focused. This observation was in agreement with a previous report on a filter-paper-based SERS substrate.[25] Figure 6b illustrates the representative SERS spectra from different regions of the Raman map. The overall relative standard deviation (RSD) of the Raman intensity on cellulose paper SERS substrate was measured to be up to 28.4%.

In contrast, the TO-nanopaper-based SERS substrate has a uniform layer of AgNPs on the flatter and smoother

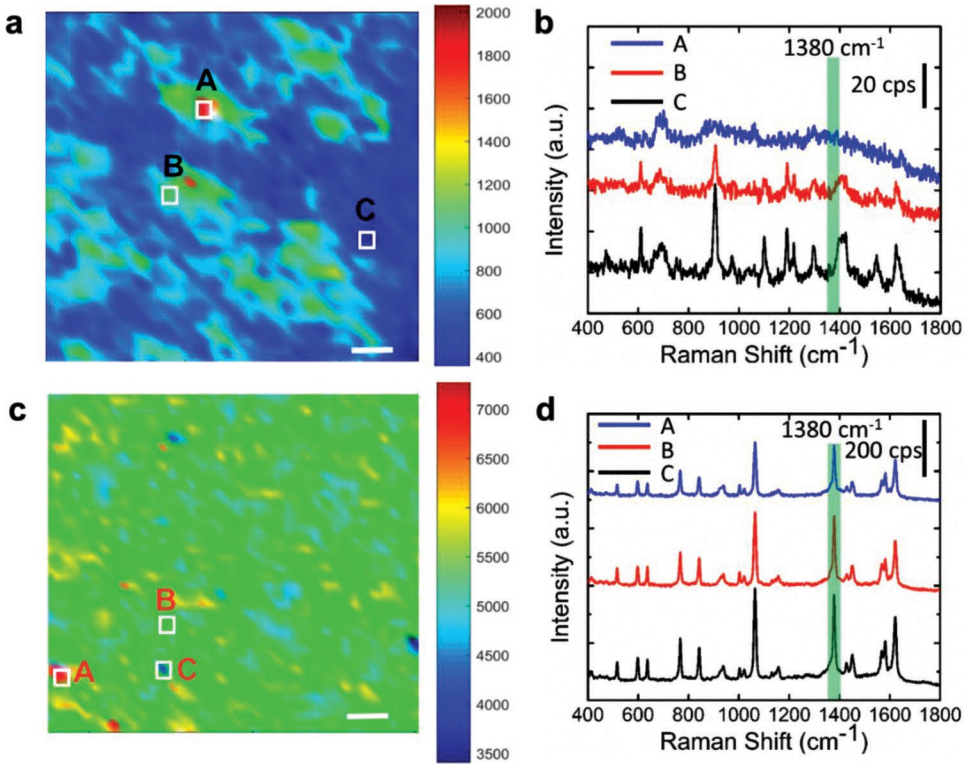

Figure 6. Spatial homogeneity measurement of the SERS signal from cellulose paper and TO-nanopaper based SERS substrates. a,c) Corresponding intensity maps of signal intensities at the 1380 cm^{-1} peak measured from a randomly selected area of 50×50 μm^2 on the cellulose paper and the TO-nanopaper substrates, respectively. b,d) The Raman spectra of 2-NT obtained from three marked spots in (a) and (c), respectively.

surface of the TO-nanopaper. As illustrated in Figure 6c, the Raman intensity map (at 1380 cm^{-1}) of a 50×50 μm^2 area on the TO-nanopaper-based SERS substrate shows much higher signal homogeneity. The representative spectra from different regions of the Raman map displayed similar peak profiles (Figure 6d). Figure S6 (Supporting Information) also shows the SERS spectral of TO-nanopaper, which were obtained based on the Raman map through randomly selected acquisitions in horizontal direction (Figure S6a, Supporting Information) and in vertical direction (Figure S6c, Supporting Information) with regular spacing (about 5 μm), respectively. The variations in the intensity of Raman spectra (at the position of 1380 cm^{-1}) showed in Figure S6b,d (Supporting Information) are very small with RSD of 5.45 and 5.60%, respectively. However, we determined the real reproducibility by calculating overall RSD from the Raman intensity at position of 1380 cm^{-1} at all 400 spectral in the Raman map. The overall RSD for TO-nanopaper is found to be ≈11%, which is significantly lower compared to cellulose paper substrate and is comparable to the signals observed from commercial Klarite SERS substrates manufactured through microfabrication techniques.[61,62] Therefore, these results further highlight that our TO-nanopaper-based SERS multiwell plate could serve as a highly consistent SERS sensing platform.

A practical SERS substrate requires both high enhancement factor and excellent spatial reproducibility.[63] Paper-based SERS substrates offer cost-effective platform for chemical and biochemical species and are particularly valuable for point-of-care analysis.[64] We summarized recent representative paper-based SERS substrates on the aspects of materials, preparation methods, EF, signal reproducibility, and analytical performance in **Table 1**. As mentioned before, the common issue for paper-based SERS device is the low spatial homogeneity of SERS intensity across the substrates,[25,26] which is attributed to nonuniform distribution of nanoplasmonic (e.g., AgNPs) structures on the porous surface. The nanocellulose paper has ultrasmooth surface and homogeneous distribution of surface chemical groups, thus providing high potential to address this issue.[30–34] In our study, we were able to report a good uniformity with 11% from 400 pixels of 50×50 μm^2 area.

Regarding the analytical performance, our TO-nanopaper SERS device has picomolar level sensitivity and EF of 1.46×10^9 which is comparable to the reported highest sensitive paper-based SERS substrates.[23] It seems that despite of high reproducibility (RSD 4% reported by Tian et al.[34]), the reported sensitivities of the nanopaper-based SERS substrates were generally low (nanomolar level), which might be due to low NPs density through employed fabrication techniques.[31–34] A recent study reported filtration-based preconcentration of analytes and achieved femtomolar level LOD.[35] However, this method requires mixing analytes with presynthesized NPs and NFC, followed by vacuum filtration to form nanopaper, which is not suitable for practical applications that require on-site sample collection and direct analytes analysis. Its overall test time could thus last for several hours to 1 d. Compared to fabrication efficiency of these paper-based SERS device, the overall device fabrication time of our device is less than 15 min, including wax printing and SILAR growth of AgNPs. It should be noted

Table 1. A list of representative paper-based SERS substrates synthesis method and SERS performance.

Paper substrates	Synthesis methods	Analytes	EF	Uniformity (RSD)	Linear range	LOD	Ref.
TO-NFC nanopaper	AgNPs in situ synthesis by SILAR	RdB, 2-NT	1.46×10^9	≤11% from 400 spots (pixels)	1×10^{-12} to 100×10^{-9} M	$<1 \times 10^{-12}$ M	This work
Whatman no. 1 cellulose filter paper	Presynthesized AuNR dropped on substrate	R6G	ND	ND	Not plotted	100×10^{-18} M (with preconcentration microfluidic unit)	[22]
Whatman no. 1 cellulose filter paper	AgNPs in situ synthesis by SILAR	RdB	1.1×10^9	4.2% for 10 different substrates (not surface uniformity)	Three different ranges from 1×10^{-12} to 100×10^{-6} M	10×10^{-12} M	[23]
Whatman no. 1 cellulose filter paper	Au NRs dropped on paper substrate	BPE	$\approx 5 \times 10^6$	15% (along the length of a fiber)	Not plotted	0.5×10^{-9} M	[25]
Chromatography cellulose paper	AgNPs, inkjet printing	R6G	2×10^5	Large variations, data not shown	ND	10×10^{-15} M μL^{-1} (10×10^{-9} M)	[26]
Whatman no. 1 cellulose filter paper	AgNPs and Au NPs ink, screen printing	R6G	8.6×10^6	≈15% (from 14 random spots)	10×10^{-12} to 10×10^{-9} M	0.11×10^{-12} M	[27]
Bacterial NFC nanopaper	Mixing graphene oxide/AgNP with NFC and dried	R6G	ND	≈21%	1×10^{-9} to 10×10^{-6} M	0.13×10^{-9} M	[32]
Bacterial NFC nanopaper	AuNPs, in situ synthesis by photoinduction	R6G	ND	ND	Not plotted	0.1×10^{-9} M	[33]
Bacterial NFC nanopaper	AuNRs and NFC mixture; infiltration to prepare substrate	R6G	ND	≈4% (from 221 pixels)	10×10^{-9} to 1×10^{-6} M	1×10^{-9} M	[34]
NFC nanopaper	AuNRs, NFC and analytes mixture; vacuum filtration to prepare substrate	R6G	ND	ND	1 to 100×10^{-9} M	10×10^{-12} M (preconcentrated via long-time infiltration)	[35]

Note: RdB = Rhodamine B; 2-NT = 2-naphthalenethiol; R6G = Rhodamine 6 G; MGITC = malachite green isothiocyanate; BPE = trans-1,2-bis(4-pyridyl)ethene; Ag = silver; Au = Gold; NP = nanoparticles; NR = nanorods; ND = not determined.

that the highly efficient SILAR growth of AgNPs in our test only took 10 min for five SILAR cycles and the reaction was conducted on room temperature. It is also possible for automation and large-scale production by using commercial platforms (such as Holmarc SILAR coating system, Holmarc Pvt. Ltd.).

The cost of transparent nanopaper production is currently much higher than that of cellulose paper (which is about $500 to $1500 ton^{-1}) due to energy- and time-consuming nanocellulose manufacturing procedures such as chemical treatment for nanocellulose preparation ($2700 ton^{-1} NFC for TEMPO-based treatment) and vacuum filtration for nanopaper preparation in our study.[65] However, it is expected that the production costs could be potentially reduced with the possibility to recycle expensive catalyst TEMPO from spent liquid.[66,67] Furthermore, the semi-industrial scale production of nanopaper operated by using roll-to-roll process from VTT Technical Research Centre and Aalto University paved the way for industrial scale production of nanopaper with more efficiency and lower cost.[68,69] Therefore, there is significant potential that nanopaper will become commercially available with more affordable cost with technology development and industrial scale production.

3. Conclusion

We reported the fabrication and testing of a TO-nanopaper-based SERS multiwell plate with high sensitivity and high signal spatial homogeneity. Comparing to the commercial cellulose filter paper and the custom-made regular nanopaper (without TEMPO oxidation), the TO-nanopaper was demonstrated to support more efficient growth of AgNPs with uniform sizes and continuous and densely arranged coverage, thanks to its large amount of surface carboxyl groups and high surface smoothness. The TO-nanopaper-based SERS multiwell plate exhibited a LOD of 1×10^{-12} M and a high EF of 1.46×10^9 for RhB detection, which highlights the promise of this SERS platform for high-performance analytical testing. The Raman mapping results showed higher spatial homogeneity (variation: 11%) of the Raman signal from the TO-nanopaper-based substrate than that of the cellulose-paper-based one. The TO-nanopaper-based SERS device represents a promising platform for high-performance SERS-based chemical and biosensing.

4. Experimental Section

Reagents and Materials: $AgNO_3$ (>99%), $NaBH_4$ (>96%), RhB (>95%), 2-NT, and ethanol (>99%) were purchased from Sigma-Aldrich (Oakville, ON, Canada). All reagents were of analytical grade and used as received without further purification. Whatman grade 1 cellulose filter paper (Catalog No. 1001125; thickness: 0.18 mm) was purchased from GE Healthcare Life Science (Pittsburgh, PA). TEMPO-oxidized NFC slurry (Catalog No. CNF-1; 1.0 wt% solid, carboxylate level 1.4 mmol g^{-1} solid, average nanofiber diameter: 10 nm) and regular (non-TEMPO-oxidized) NFC slurry (Catalog No. TOCN-9; 3.0 wt% solid, average nanofiber diameter: 50 nm) were purchased from the Process Development Center at University of Maine. The nanofibers dimensions were further confirmed by SEM (Figure S1, Supporting Information). Polyethylene

terephthalate (PET) film (Catalog No. 8567K12) was purchased from McMaster-CARR.

Nanopaper Preparation: In a typical nanopaper preparation experiment, TEMPO-oxidized NFC solution was prepared by suspending the original slurry in distilled water to a final nanofiber content of 0.1 wt%. The suspension was stirred for 2 h at 1000 rpm. 50 g of the prepared suspension was vacuum-filtered for 6 h with a PVDF filter membrane (VVLP09050, EMD Millipore Corporation, pore size: 0.1 µm) on a glass filter holder. After the filtration, a piece of wet gel "cake" containing all the NFC was formed on top of the filter membrane. The gel "cake" (diameter: 7 cm) was carefully removed from the filter membrane, sandwiched by a PET film and a Whatman grade 1 filter paper and then by two Teflon boards. Next, the stack was placed on a hot press machine (model 311011D, Carver Inc., Wabash, IN), pressed and dried under a pressure of 2.6 MPa at 90 °C for 10 min. The dried TO-nanopaper has a thickness of 20 µm. Regular nanopaper was also prepared from the regular NFC slurry (without TEMPO oxidization) using a similar filtration and pressing procedure.

Fabrication of Nanopaper-Based SERS Multiwell Plate: For comparison, paper-based multiwell plates were fabricated through wax printing on three types of paper substrate, including the Whatman grade 1 cellulose filter paper, regular nanopaper, and TO-nanopaper, and then synthesized AgNPs on them. For wax printing, the pattern of a 3×3 multiwell plate (well diameter: 6 mm; pitch: 9 mm) was designed using AutoCAD 2016 (Autodesk, San Rafael, CA), and then printed onto a 30×30 mm^2 paper substrate using a solid wax printer (Xerox ColorQube 8570N, Xerox, Mississauga, ON, Canada). The solid wax pattern forms individual hydrophilic barriers on the top surface of the paper substrate, which can effectively confine the solution added to a nanopaper well coated with AgNPs. Figure 1b-i shows a TO-nanopaper-based multiwell plate before AgNP growth.

A modified SILAR process was adopted for AgNP growth on multiwell plates made from three types of paper.[23] The chemical reaction involved in the process is expressed by

$$AgNO_3 + NaBH_4 \rightarrow Ag + \frac{1}{2}H_2 + \frac{1}{2}B_2H_6 + NaNO_3 \quad (2)$$

where $AgNO_3$ and $NaBH_4$ serve as the silver precursor and the reductant, respectively.

Figure 1a shows the scheme of the SILAR process on TO-nanopaper. In brief, the multiwell plate was immersed in an $AgNO_3$ solution for 30 s and washed with distilled water for 30 s. Next, the substrate was immersed into a $NaBH_4$ solution for 30 s and washed with distilled water for 30 s. To this point, one SILAR cycle was completed, which took ≈2 min in total. The SILAR process was repeated for multiple cycles to form uniform coverage of AgNPs on paper. As the wax patterns on the paper surface are hydrophobic, the reaction only happened on the surface of the paper wells. Optimum growth conditions, including the reagent concentrations and the number of SILAR circles, were experimentally determined by measuring the SERS signal enhancement (see results in Section 2.2). Finally, the paper-SERS device was dried in a convection oven at 60 °C for 15 min and stored in dark condition before use. Figure 1b-ii shows a TO-nanopaper-based multiwell plate coated with the AgNPs. No AgNP coverage was observed on the wax patterns.

Characterization of AgNP-Coated Paper Substrates: The surface morphologies of the three types of AgNP-coated paper substrate were characterized using a SEM (Inspect F-50, FEI Co., Hillsboro, OR) coupled with an EDS (60 mm^2 octane silicon drift detector, EDAX Inc., Mahwah, NJ) operating at 10 kV. The absorption spectra of the pristine and AgNP-coated TO-nanopaper were measured on a UV–vis spectrometer (SpectraMax M5, Molecular Devices, Sunnyvale, CA). XPS-based elemental analysis of the AgNP-coated TO-nanopaper was performed on a monochromatic Al K-Alpha X-ray photoelectron spectrometer (Thermo Scientific, Waltham, MA). Three scans were collected for each sample in the range of 0–1350 eV with an incremental step of 1 eV. Elemental high-resolution scanning was conducted under a step size of 0.1 eV and repeated for five times. The XPS peak fittings were performed through the Thermo Avantage software (version 4.6; Thermo Fisher Scientific Inc.), and the spectral energies were calibrated by setting the C—C binding energy at 284.8 eV.

SERS Measurement: To test the SERS activity on a SERS paper well, RhB and 2-NT were dissolved in 100% ethanol at ten times dilutions of 10×10^{-15} to 10×10^{-6} M. In every experiment, 2 µL of the analyte solution was dropped on the SERS paper well and further left to dry in air. Raman spectra were collected using a confocal Raman microscope (SENTERRA, Bruker Inc., Karlsruhe, Germany) with a 633 nm laser and a 20× objective. The size of the focused laser spot on the sample was ≈25 µm in diameter. The spectrometer provides a Raman spectrum in the region of 376 to 1800 cm^{-1} with a spectral resolution of 3 cm^{-1}. The Raman spectra were averaged from two measurements. Spectral data were collected using the OPUS spectroscopy software (Bruker Inc., Karlsruhe, Germany). A baseline correction routine was performed to obtain the final spectrum of each measurement with the background spectrum subtracted.

Raman mapping experiments were conducted over an area of 50×50 µm^2 on a SERS paper well with a 2-NT solution of 10^{-6} M added and dried. Raman spectra were acquired with a spatial resolution of 1.25 µm, both along *x* and *y*-axes of the scanning area. The Raman peak intensity at ≈1380 cm^{-1} was used to form a spatial Raman map because this peak is well separated from other features of the 2-NT spectrum, thus making it easier to evaluate its intensity over the background.

Supporting Information

Supporting Information is available from the Wiley Online Library or from the author.

Acknowledgements

L.C. and B.Y. contributed equally to this work. The authors gratefully acknowledge the support from the Natural Sciences and Engineering Research Council of Canada (Grant Nos. RGPIN-06374-2017 and RGPAS-507980-2017), University of Toronto, and McGill University. The authors also acknowledge the financial supports from the Chinese Scholarship Council to P.S. The authors are thankful to Dr. Ghulam Jalani for providing assistances in Raman instrument training and giving advices in result analysis.

Conflict of Interest

The authors declare no conflict of interest.

Keywords

chemical analysis and biosensing, nanofibrillated cellulose, nanopaper, paper-based device, surface-enhanced Raman scattering (SERS)

Received: August 2, 2019
Revised: October 8, 2019
Published online: November 13, 2019

[1] S. Schlücker, *Angew. Chem., Int. Ed.* **2014**, *53*, 4756.
[2] S. Zeng, D. Baillargeat, H.-P. Ho, K.-T. Yong, *Chem. Soc. Rev.* **2014**, *43*, 3426.
[3] J. N. Anker, W. P. Hall, O. Lyandres, N. C. Shah, J. Zhao, R. P. Van Duyne, *Nat. Mater.* **2008**, *7*, 442.
[4] P. L. Stiles, J. A. Dieringer, N. C. Shah, R. P. V. Duyne, *Annu. Rev. Anal. Chem.* **2008**, *1*, 601.
[5] J. Kneipp, H. Kneipp, K. Kneipp, *Chem. Soc. Rev.* **2008**, *37*, 1052.
[6] M. Fan, A. G. Brolo, *Phys. Chem. Chem. Phys.* **2009**, *11*, 7381.

[7] S. L. Kleinman, E. Ringe, N. Valley, K. L. Wustholz, E. Phillips, K. A. Scheidt, G. C. Schatz, R. P. Van Duyne, *J. Am. Chem. Soc.* **2011**, *133*, 4115.
[8] Y. He, S. Su, T. Xu, Y. Zhong, J. A. Zapien, J. Li, C. Fan, S. T. Lee, *Nano Today* **2011**, *6*, 122.
[9] K. Sivashanmugan, J. D. Liao, B. H. Liu, C. K. Yao, S. C. Luo, *Sens. Actuators, B* **2015**, *207*, 430.
[10] X. Chen, C. H. Cui, Z. Guo, J. H. Liu, X. J. Huang, S. H. Yu, *Small* **2011**, *7*, 858.
[11] W. Ye, Y. Chen, F. Zhou, C. Wang, Y. Li, *J. Mater. Chem.* **2012**, *22*, 18327.
[12] M. Green, F. M. Liu, *J. Phys. Chem. B* **2003**, *107*, 13015.
[13] A. Hakonen, M. Svedendahl, R. Ogier, Z.-J. Yang, K. Lodewijks, R. Verre, T. Shegai, P. O. Andersson, M. Kall, *Nanoscale* **2015**, *7*, 9405.
[14] L. Zhang, X. Lang, A. Hirata, M. Chen, *ACS Nano* **2011**, *5*, 4407.
[15] X. Liu, Y. Shao, Y. Tang, K.-F. Yao, *Sci. Rep.* **2014**, *4*, 5835.
[16] J. Zhang, X. Zhang, C. Lai, H. Zhou, Y. Zhu, *Opt. Express* **2014**, *22*, 21157.
[17] A. W. Martinez, S. T. Phillips, M. J. Butte, G. M. Whitesides, *Angew. Chem., Int. Ed.* **2007**, *46*, 1318.
[18] A. W. Martinez, S. T. Phillips, G. M. Whitesides, *Anal. Chem.* **2010**, *82*, 3.
[19] A. K. Yetisen, M. S. Akram, C. R. Lowe, *Lab Chip* **2013**, *13*, 2210.
[20] D. M. Cate, J. A. Adkins, J. Mettakoonpitak, C. S. Henry, *Anal. Chem.* **2015**, *87*, 19.
[21] M. Chen, H. Yang, L. Rong, X. Chen, *Analyst* **2016**, *141*, 5511.
[22] A. Abbas, A. Brimer, J. M. Slocik, L. Tian, R. R. Naik, S. Singamaneni, *Anal. Chem.* **2013**, *85*, 3977.
[23] W. Kim, Y.-H. Kim, H.-K. Park, S. Choi, *ACS Appl. Mater. Interfaces* **2015**, *7*, 27910.
[24] Y. Zhu, M. Li, D. Yu, L. Yang, *Talanta* **2014**, *128*, 117.
[25] C. H. Lee, M. E. Hankus, L. Tian, P. M. Pellegrino, S. Singamaneni, *Anal. Chem.* **2011**, *83*, 8953.
[26] W. W. Yu, I. M. White, *Anal. Chem.* **2010**, *82*, 9626.
[27] L. L. Qu, Q. X. Song, Y. T. Li, M. P. Peng, D. W. Li, L. X. Chen, J. S. Fossey, Y. T. Long, *Anal. Chim. Acta* **2013**, *792*, 86.
[28] E. Morales-Narváez, H. Golmohammadi, T. Naghdi, H. Yousefi, U. Kostiv, D. Horák, N. Pourreza, A. Merkoçi, *ACS Nano* **2015**, *9*, 7296.
[29] F. Hoeng, A. Denneulin, J. Bras, *Nanoscale* **2016**, *8*, 13131.
[30] L. Hu, G. Zheng, J. Yao, N. Liu, B. Weil, M. Eskilsson, E. Karabulut, Z. Ruan, S. Fan, J. T. Bloking, *Energy Environ. Sci.* **2013**, *6*, 513.
[31] H. Wei, K. Rodriguez, S. Renneckar, W. Leng, P. J. Vikesland, *Analyst* **2015**, *140*, 5640.
[32] E. Rodríguez-Sevilla, G. V. Vázquez, E. Morales-Narváez, *Adv. Opt. Mater.* **2018**, *6*, 1800548.
[33] X. Zhou, Z. Zhao, Y. He, Y. Ye, J. Zhou, J. Zhang, Q. Ouyang, B. Tang, X. Wang, *Cellulose* **2018**, *25*, 3941.
[34] L. Tian, Q. Jiang, K. K. Liu, J. Luan, R. R. Naik, S. Singamaneni, *Adv. Mater. Interfaces* **2016**, *3*, 1600214.
[35] S. Zhang, R. Xiong, M. A. Mahmoud, E. N. Quigley, H. Chang, M. El-Sayed, V. V. Tsukruk, *ACS Appl. Mater. Interfaces* **2018**, *10*, 18380.
[36] K. G. Stamplecoskie, J. S. Manser, *ACS Appl. Mater. Interfaces* **2014**, *6*, 17489.
[37] T. Saito, S. Kimura, Y. Nishiyama, A. Isogai, *Biomacromolecules* **2007**, *8*, 2485.
[38] T. Saito, A. Isogai, *Carbohydr. Polym.* **2005**, *61*, 183.
[39] J. Song, N. L. Birbach, J. P. Hinestroza, *Cellulose* **2012**, *19*, 411.
[40] S. Agnihotri, S. Mukherji, S. Mukherji, *RSC Adv.* **2014**, *4*, 3974.
[41] I. M. Shaikh, S. D. Sartale, *J. Raman Spectrosc.* **2018**, *49*, 1274.
[42] D. Li, D.-W. Li, Y. Li, J. S. Fossey, Y.-T. Long, *J. Mater. Chem.* **2010**, *20*, 3688.
[43] K. G. Stamplecoskie, J. C. Scaiano, V. S. Tiwari, H. Anis, *J. Phys. Chem. C* **2011**, *115*, 1403.
[44] M. J. Banholzer, J. E. Millstone, L. Qin, C. A. Mirkin, *Chem. Soc. Rev.* **2008**, *37*, 885.
[45] L. Mulfinger, S. D. Solomon, M. Bahadory, A. V. Jeyarajasingam, S. A. Rutkowsky, C. Boritz, *J. Chem. Educ.* **2007**, *84*, 322.
[46] Y.-T. Yen, T.-Y. Lu, Y.-C. Lee, C.-C. Yu, Y.-C. Tsai, Y.-C. Tseng, H.-L. Chen, *ACS Appl. Mater. Interfaces* **2014**, *6*, 4292.
[47] L. M. Liz-Marzán, *Mater. Today* **2004**, *7*, 26.
[48] B. K. Canfield, S. Kujala, K. Jefimovs, T. Vallius, J. Turunen, M. Kauranen, *J. Opt. A: Pure Appl. Opt.* **2005**, *7*, S110.
[49] P. Taneja, P. Ayyub, R. Chandra, *Phys. Rev. B* **2002**, *65*, 245412.
[50] H. Yockell-Lelièvre, E. F. Borra, A. M. Ritcey, L. Vieira da Silva, *Appl. Opt.* **2003**, *42*, 1882.
[51] Y. Saito, J. J. Wang, D. N. Batchelder, D. A. Smith, *Langmuir* **2003**, *19*, 6857.
[52] S. C. Dixon, J. A. Manzi, M. J. Powell, C. J. Carmalt, I. P. Parkin, *ACS Appl. Nano Mater.* **2018**, *1*, 3724.
[53] M. Futamata, Y.-Y. Yu, T. Yanatori, T. Kokubun, *J. Phys. Chem. C* **2010**, *114*, 7502.
[54] Y. Xue, X. Li, H. Li, W. Zhang, *Nat. Commun.* **2014**, *5*, 4348.
[55] L. Tian, J. Luan, K.-K. Liu, Q. Jiang, S. Tadepalli, M. K. Gupta, R. R. Naik, S. Singamaneni, *Nano Lett.* **2016**, *16*, 609.
[56] H. K. Lee, Y. H. Lee, Q. Zhang, I. Y. Phang, J. M. R. Tan, Y. Cui, X. Y. Ling, *ACS Appl. Mater. Interfaces* **2013**, *5*, 11409.
[57] F. Sun, D. D. Galvan, P. Jain, Q. Yu, *Chem. Commun.* **2017**, *53*, 4550.
[58] S.-H. Yeh, K.-H. Chou, R.-J. Yang, *Lab Chip* **2016**, *16*, 925.
[59] A. Jajack, I. Stamper, E. Gomez, M. Brothers, G. Begtrup, J. Heikenfeld, *PLoS One* **2019**, *14*, e0210286.
[60] E. C. Le Ru, E. Blackie, M. Meyer, P. G. Etchegoin, *J. Phys. Chem. C* **2007**, *111*, 13794.
[61] N. M. B. Perney, J. J. Baumberg, M. E. Zoorob, M. D. B. Charlton, S. Mahnkopf, C. M. Netti, *Opt. Express* **2006**, *14*, 847.
[62] J. Li, C. Chen, H. Jans, X. Xu, N. Verellen, I. Vos, Y. Okumura, V. V. Moshchalkov, L. Lagae, P. Van Dorpe, *Nanoscale* **2014**, *6*, 12391.
[63] D.-K. Lim, K.-S. Jeon, J.-H. Hwang, H. Kim, S. Kwon, Y. D. Suh, J.-M. Nam, *Nat. Nanotechnol.* **2011**, *6*, 452.
[64] S. M. Restaino, I. M. White, *Anal. Chim. Acta* **2019**, *1060*, 17.
[65] Z. Fang, H. Zhu, C. Preston, L. Hu, *Transl. Mater. Res.* **2014**, *1*, 015004.
[66] A. K. Suresh, M. M. Sharma, T. Sridhar, *Ind. Eng. Chem. Res.* **2000**, *39*, 3958.
[67] Y. Habibi, L. A. Lucia, O. J. Rojas, *Chem. Rev.* **2010**, *110*, 3479.
[68] T. Tammelin, U. Hippi, A. Salminen, *WO 2013/060934 A2*, **2013**.
[69] https://www.vttresearch.com/services/bioeconomy/biobased-materials/nanocellulose-film, (accessed: July 2019).